Journal of Colloid and Interface Science 637 (2023) 408–420

Contents lists available at ScienceDirect

Journal of Colloid and Interface Science

journal homepage: www.elsevier.com/locate/jcis

Poly(ionic liquid) nanovesicles *via* polymerization induced self-assembly and their stabilization of Cu nanoparticles for tailored CO_2 electroreduction

Xuefeng Pan [a,g], Zdravko Kochovski [a], Yong-Lei Wang [a], Radwan M. Sarhan [a,d], Eneli Härk [a], Siddharth Gupta [b,c], Sasho Stojkovikj [b,c], Gumaa A. El-Nagar [b,d,*], Matthew T. Mayer [b], Robin Schürmann [e], Jérôme Deumer [e], Christian Gollwitzer [e], Jiayin Yuan [f,*], Yan Lu [a,g,*]

[a] Department for Electrochemical Energy Storage, Helmholtz-Zentrum Berlin für Materialien und Energie, Hahn-Meitner-Platz 1, 14109 Berlin, Germany
[b] Helmholtz Young Investigator Group: Electrochemical Conversion, Helmholtz-Zentrum Berlin für Materialien und Energie, Hahn-Meitner-Platz 1, 14109 Berlin, Germany
[c] Institut für Chemie und Biochemie, Freie Universität Berlin, Arnimallee 22, D-14195 Berlin, Germany
[d] Chemistry Department, Faculty of Science, Cairo University, Egypt
[e] Physikalisch-Technische Bundesanstalt (PTB), Abbestr. 2-12, 10587 Berlin, Germany
[f] Department of Materials and Environmental Chemistry (MMK), Stockholm University, Svante Arrhenius väg 16C, 10691 Stockholm, Sweden
[g] Institute of Chemistry, University of Potsdam, Karl-Liebknecht-Str. 24-25, 14476 Potsdam, Germany

GRAPHICAL ABSTRACT

This study casts new aspects on using nanostructured PILs as new electrocatalyst supports in CO_2 conversion to C_1 products.

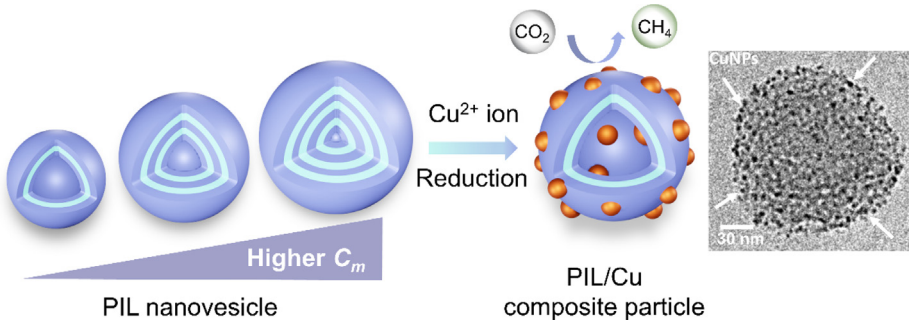

ARTICLE INFO

Article history:
Received 7 November 2022
Revised 18 January 2023
Accepted 20 January 2023
Available online 21 January 2023

Keywords:
Poly(ionic liquid)
Nanovesicles
Polymerization-induced self-assembly
Nanoparticles
CO_2 electroreduction

ABSTRACT

Herein, we report a straightforward, scalable synthetic route towards poly(ionic liquid) (PIL) homopolymer nanovesicles (NVs) with a tunable particle size of 50 to 120 nm and a shell thickness of 15 to 60 nm *via* one-step free radical polymerization induced self-assembly. By increasing monomer concentration for polymerization, their nanoscopic morphology can evolve from hollow NVs to dense spheres, and finally to directional worms, in which a multilamellar packing of PIL chains occurred in all samples. The transformation mechanism of NVs' internal morphology is studied in detail by coarse-grained simulations, revealing a correlation between the PIL chain length and the shell thickness of NVs. To explore their potential applications, PIL NVs with varied shell thickness are *in situ* functionalized with ultra-small ($1 \sim 3$ nm in size) copper nanoparticles (CuNPs) and employed as electrocatalysts for CO_2 electroreduction. The composite electrocatalysts exhibit a 2.5-fold enhancement in selectivity towards C_1 products (*e.g.*, CH_4), compared to the pristine CuNPs. This enhancement is attributed to the strong electronic

* Corresponding authors.
E-mail addresses: gumaa.el-nagar@helmholtz-berlin.de (G.A. El-Nagar), jiayin.yuan@mmk.su.se (J. Yuan), yan.lu@helmholtz-berlin.de (Y. Lu).

https://doi.org/10.1016/j.jcis.2023.01.097
0021-9797/© 2023 The Authors. Published by Elsevier Inc.
This is an open access article under the CC BY license (http://creativecommons.org/licenses/by/4.0/).

interactions between the CuNPs and the surface functionalities of PIL NVs. This study casts new aspects on using nanostructured PILs as new electrocatalyst supports in CO_2 conversion to C_1 products.
© 2023 The Authors. Published by Elsevier Inc. This is an open access article under the CC BY license (http://creativecommons.org/licenses/by/4.0/).

1. Introduction

Polymer nanovesicles (NVs) self-assembled from amphiphilic polymers have aroused intensive interest in diverse research areas such as drug delivery, cell mimicking, nanoreactors, and water remediation.[1–5] Owing to their inherent hollow shape, polymer NVs possess light weight, large surface area, and a unique compartmentalized cavity.[6–8] These structural characteristics are directly associated with their mechanical stability, membrane permeability, and encapsulating capability, which impact their material performance.[9–11] For instance, when it comes to nanoreactors, the tiny cavity of the NVs is beneficial for achieving higher reaction rates and potentially better catalytic performance due to the shortened transport distance for the reaction medium and reactants.[12,13] Recently, various synthetic approaches toward precise control over the size of NVs have been developed, including the solvent exchange method, template-assisting route, and microfluidics.[14–17] However, from the applicative perspective, the involvement of organic solvents and/or complex devices in the above-mentioned approaches is undesirable and may limit their future practical use.

From the structural perspective, in addition to the dimension of the NVs, the shell thickness is essential in regulating the shape robustness and mass transport into and out of NVs. As the majority of vesicles are made up of amphiphilic block polymers *via* the default concept of block copolymer self-assembly, it is common to alter the relative and absolute length scale of the hydrophilic and hydrophobic blocks to dictate the shell thickness.[18,19] However, the tedious, time-intensive synthetic protocols for block copolymers *via* multistep polymerizations are the apparent dilemma and bottleneck for real-life applications. By contrast, efforts have been rarely directed to tailor shell thickness by the homopolymer approach, which is often ignored in the NV synthesis for lack of qualified homopolymers and the fuzzy boundary between hydrophobic and hydrophilic moieties within the same repeating unit.

Poly(ionic liquid)s (PILs), as a fascinating group of functional ionic polymers, have been actively employed in multiple research areas including ionic liquids (ILs), polymer science, materials chemistry, sensing technology, and analytic chemistry, just to name a few.[20–25] In terms of molecular structure design, a series of PIL homopolymers has been fabricated from diverse IL monomers; these PIL homopolymers typically carry cationic backbones (*e.g.*, polyimidazolium, polypyridinium, and polyphosphonium) with side alkyl chains of various lengths and counter anions (*e.g.*, halides, acetate, and hexafluorophosphate).[26,27] The amphiphilicity of PILs is readily modulated by the choice of the alkyl chain length and counterion type, without varying the synthetically complex backbone.[28–30] Taking advantage of a large number of existent amphiphilic IL monomers, a couple of PIL homopolymers in vesicular nanostructures have been indeed made.[31] The microphase separation of PILs during their polymerization gives rise to the simultaneous formation of NVs, that is to say, the chemical polymerization drives the physical self-assembly process. This straightforward technique for polymer assembly is often defined as "polymerization induced self-assembly" (PISA), which due to its easiness in implementation has been prevailing for preparing nanoparticles of a rich library of morphologies at a broad polymer concentration window.[32] Nevertheless, the essential factors affecting the internal structures and self-assembled morphologies of PILs *via* PISA remain mysterious and lack in-depth investigation.

In addition to the prominent advantages in vesicle assembly, PILs find versatile applications including drug delivery, catalyst supports, and CO_2 sorption/conversion.[26,33–35] In light of the growing demand for clean energy sources, the electrochemical conversion of CO_2 (CO_2ER) into valuable chemicals provides an auspicious approach to mitigating the negative impacts of excess CO_2 emissions. [36–38] A primary technological challenge is to design selective electrocatalysts with high stability and production rates. Tackling the undesired parasitic hydrogen evolution reaction (HER) is crucial to mitigate the aforementioned-challenges.[39,40] Copper (Cu) is the only known metal that enables CO_2 electroreduction to high-value hydrocarbons (*e.g.,* CH_4 and C_2H_4) with considerable production rates, despite its poor selectivity towards specific products.[41–43] A variety of approaches, including surface functionalization, surface nano-structuring, and alloying, have been used to enhance the selectivity of Cu catalysts.[44–46] Very recently, copper nanoparticles (CuNPs) functionalized with PILs have been used to tune CO_2ER selectivity towards hydrocarbons.[47] In addition, PILs are an excellent stabilizer and carrier for metal nanoparticles, and are capable of efficiently tailoring their particle size.[48–51]

Herein, we finely modulated the CO_2ER selectivity of CuNPs by *in situ* synthesis and anchoring them into structurally well-defined PIL NVs with specific surface functional groups. Concretely, we first systematically investigated the morphological transformation of PIL homopolymer NVs *via* free radical polymerization by varying the concentration of monomer 3-*n*-decyl-1-vinylimidazolium bromide ($3 \leq C_m \leq 48$ mg/mL) (Scheme 1). Intriguingly, multilamellar NVs with controllable overall size and shell thickness were obtained *via* PISA, and the corresponding formation mechanism was proposed and validated *via* coarse-grained simulations. As a step forward to explore the utilization of such exquisitely constructed nanostructures, the PIL NVs with different shell thicknesses were *in situ* decorated by uniform ultra-small CuNPs of $1 \sim 3$ nm in size for CO_2ER. The synthesized hollow PIL/Cu composite particles exhibited an enhanced selectivity towards C_1 products, especially CH_4 as a crucial chemical feedstock. Moreover, quasi *in situ* X-ray photoelectron spectroscopy has been adopted to probe the surface speciation changes of the prepared PIL/Cu composite catalyst and correlating them to the CO_2ER processes.

2. Materials and methods

2.1. Chemicals

1-Vinylimidazole (99 %), 1 bromodecane (99 %), diethyl ether (≥99 %), methanol (≥99 %), 2,6-di-*tert*-butyl-4-methylphenol (BHT, ≥99 %), copper (II) acetate monohydrate ($CuAc_2{\cdot}H_2O$), and hydrazine hydrate (N_2H_4, 35 wt%) solution in water were purchased from Sigma-Aldrich. 2,2′-Azobis[2-methyl-N-(2-hydroxyethyl) propionamide] (VA86, ≥99 %) was purchased from FUJIFILM Wako Chemicals. Ultrapure water with a resistance of 18.20 MΩ·cm was purified using the Thermo Scientific Barnstead GenPurex CAD Plus system). 2-propanol (≥99.8 wt%), sulfuric acid (H_2SO_4, ≥98 wt%, EMSURE® purity), and potassium hydrogen carbonate ($KHCO_3$, 99.7–100.5 wt% ACS, EMSURE® purity) were pur-

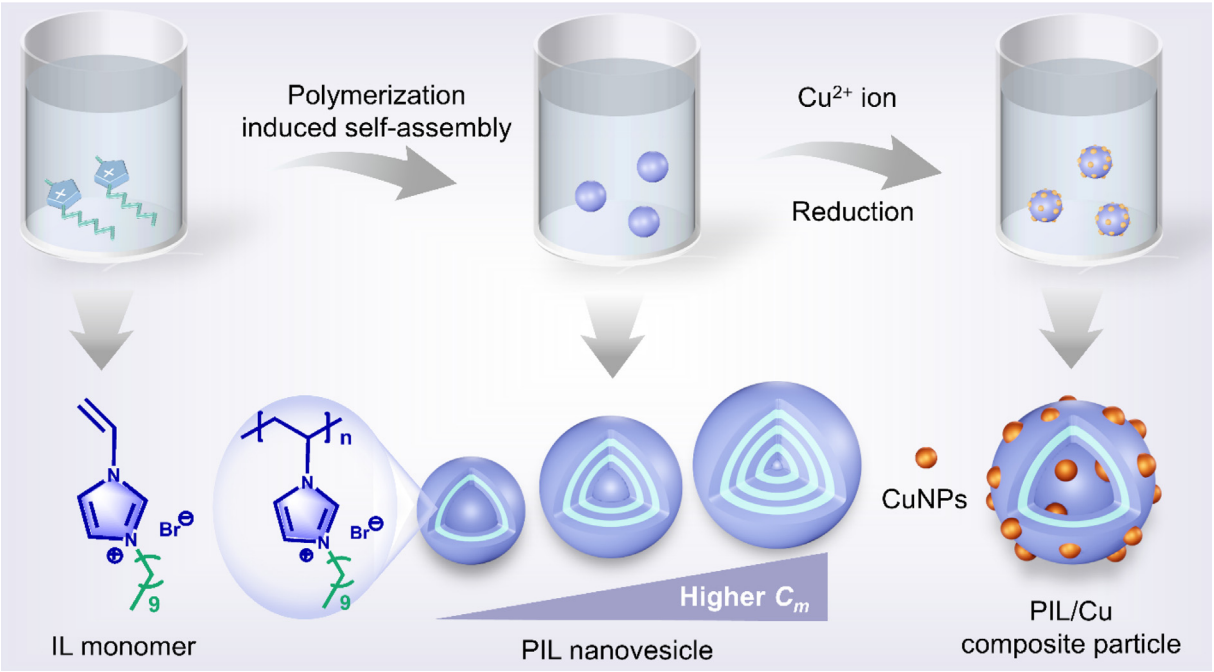

Scheme 1. Synthetic scheme of PIL NVs from its IL monomer at varied concentrations and their functionalization by CuNPs.

chased from Merck. Carbon dioxide (CO_2) gas with 4.8 purity was purchased from Linde. All chemicals were used without any further purification.

2.2. Synthesis of the IL monomer

The synthesis of the IL monomer 3-*n*-decyl-1-vinylimidazolium bromide was follow our previous report,[52] and briefly described as follows. 0.1 mol of 1-vinylimidazole and 10 mL of methanol were loaded into a 100 mL of flask. 0.1 mol of *n*-decyl bromide and 50 mg of inhibitor (BHT) were introduced to the solution. The mixture was stirred at 60 °C in an oil bath for 15 h. After cooling down, the reaction mixture was slowly added into an excess amount of diethyl ether. Then, the supernatant layer was removed and the precipitate was washed with diethyl ether 5 times. Finally, the obtained viscous liquid was dried into a brown solid under vacuum overnight to completely remove the residual solvent. The yield is *ca.* 34 %.

2.3. Synthesis of PIL NVs

In a typical run, various amounts of monomer (0.3–4.8 g) were dissolved in 100 mL of water in a 250 mL of Schlenk flask. The monomer solution was mixed with 50 mg of initiator (VA86) for *ca.* 30 min under magnetic stirring at 250 rpm. The mixture was completely deoxygenated by five cycles of the freeze–pumpthaw procedure. Subsequently, the mixture was continuously stirred at 75 °C in an oil bath overnight. After cooling down, the final colloid dispersion was exhaustively dialyzed against deionized water until the conductivity of water is below 3 μS/cm. The PIL dispersion was collected and stored in the fridge at 4 °C for further use. The PIL nanovesicles (termed "NVs") and solid nanospheres (termed "SNSs") were first prepared at a monomer concentration (C_m) of 12 and 24 mg/mL respectively, according to their morphology observed in TEM characterization. To calculate the polymerization yield (Y), the desired amount of PIL dispersion at a given C_m (V mL) after dialysis was contained in a clean dry vial and placed in an oven at 90 °C until its weight was kept constant (W). Each sample was repeated 5 times to calculate the average value. Therefore, Y can be determined by the following equation (1):

$$Y = \frac{V \times c_m - W}{V \times c_m} \times 100\% \quad (1)$$

2.4. Synthesis of PIL/Cu composite particles

The facile synthesis of colloidal PIL/Cu composite particles was conducted based on our recent study.[53] For PIL NVs ($C_m \sim 12$ mg/mL), the colloidal dispersion (4 mL, 10 mg/mL) was diluted with 32 mL of deionized water. Then a fresh $CuAc_2$ solution (4 mL, 10 mg/mL) was slowly added to the dispersion under stirring. After stirring at 250 rpm at room temperature for 4 h, an aqueous N_2H_4 solution (0.4 mL, 35 wt%) was quickly injected into the mixture. The color of the solution turned from light blue to pink. Afterwards, the solution was placed in an oil bath under stirring at 250 rpm at 80 °C overnight to complete the reduction. The color of the solution gradually changed to wine-like. After cooling down, the dispersion was sonicated again for 20 min. Subsequently, the dispersion was filtered off using a syringe with a filter (an average pore size of 1.2 μm) to remove any big aggregates. After centrifugation at 8500 rpm for 30 min and washing with fresh water, the precipitated PIL/Cu composite particles were redispersed in 25 mL of fresh water before further use. For PIL SNSs ($C_m \sim 24$ mg/mL), the synthesized dispersion (2 mL, 20 mg/mL) was used for synthesis of copper nanoparticles (CuNPs) in the same manner as mentioned above. For comparison, the pristine CuNPs were also prepared in the same way without any PIL templates. CuNP-decorated NVs and SNSs are denoted as NVs/Cu and SNSs/Cu, respectively.

2.5. CO_2 electrochemical reduction

Electrode preparation by spray coating: the as-prepared pristine CuNPs and PIL/Cu dispersions (*ca.* 4 mg/mL) were deposited onto a Freudenberg H1C49 gas diffusion layers (GDLs, 180 μm in thickness) using an ultrasonic atomizer (Sonaer 130 kHz Low Flow tapered tip atomizer) was used in conjunction with a focusing

plume shaper LF130K). The GDLs were placed on a hot plate (150 °C) while maintaining a distance of 15 cm from the nozzle tip. The dispersions were pumped through the nozzle using a Harvard Apparatus syringe pump at a flow rate of 0.5 mL/min. The compressed air supplied to the nozzle was at a pressure of 0.5 bar.

The CO_2 electrochemical reduction (CO_2ER) tests were performed in an H-type two-compartment electrochemical cell filled with 0.1 M $KHCO_3$ aqueous solution. The cathodic compartment was continuously purged with CO_2 gas at a flow rate of 20 mL/min. The as-prepared pristine CuNPs and PIL/Cu composite particles deposited GDL substrate acts as a working electrode fully immersed in the electrolyte, while Pt wire and Ag/AgCl were used as counter and reference electrodes, respectively. The electrochemical bias was provided using SP-200 potentiostat (Biologic) under chronoamperometry mode. 85 % of ohmic resistance (iR) was compensated automatically and all applied potentials were converted with respect to the Reversible Hydrogen Electrode (RHE). The cathodic gaseous products (H_2, CO, CH_4, and C_2H_4) were quantified using an online gas chromatograph (GC, Thermo Scientific) equipped with a flame ionization detector (FID) and a pulse discharge detector (PDD). The quantification interval was 10 min. Liquid products contained in the electrolyte were quantified using a high-performance liquid chromatography (HPLC) with a UV detector for the non-volatile ($HCOO^-$) and head-space gas chromatography (GC-HS) with FID detector for the volatile ones (*e.g.*, alcohols). A more detailed description of the electrochemical setup and quantification methods can be found in our previous report.[54]

2.6. Characterization methods

Nuclear magnetic resonance (NMR): ^{1}H NMR spectra were recorded at room temperature using a Bruker DPX-400 spectrometer operating at 400 MHz. Dimethyl sulfoxide-d_6 (DMSO d_6) was used as a solvent to dissolve both the IL monomer and the corresponding PIL.

Differential scanning calorimetry (DSC): DSC measurements were conducted on a Netzsch Phoenix F204 instrument at a heating rate of 10 K min^{-1} under an N_2 flow.

Gel permeation chromatography (GPC): Number-average molecular weight (M_n) and molecular weight distributions of PIL samples were determined by GPC. The GPC equipment is equipped with a PSS SECcurity 1260 autosampler injector, a PSS SECcurity 1260 HPLC pump, and a PSS SECcurity 1260 differential refractometer (RID) detector using PSS columns (PSS GRAM, 10 mm, Guard + 10 0 Å + 2 × 10,000 Å). The eluent is *N*, *N*-dimethylacetamide (DMAc) containing 10 g/L of lithium bromide (LiBr) at a flow rate of 1.0 mL/min at 70 °C.[55] The PIL powders after freeze-drying were first dissolved in eluent and kept shaking at 50 °C for *ca.* 1 h to ensure complete dissolution. Afterwards, the solutions (*ca.* 3 mg/mL) were left overnight at room temperature for equilibration. The as-prepared solutions were filtered through a PTFE syringe filter (an average pore size of 1.0 μm) before injection. The M_n and its distributions were calculated using linear polystyrene standards (M_n = 470–2520000 g/mol) for calibration by a PSS WinGPC UniChrom Version 8.4 software.

Dynamic light scattering (DLS): The average hydrodynamic diameter (D_h) and distributions were determined by using a Malvern Zetasizer Nano ZS. The scattered light was detected at an angle of 173°.

Scanning electron microscopy (SEM): The morphologies of the PIL samples were recorded on a LEO GEMINI 1530 microscope operated at 3 kV. All the samples were coated with a thin carbon layer (*ca.* 5 nm) before measurement.

Transmission electron microscopy (TEM): Conventional TEM, high-resolution TEM (HRTEM), and cryogenic transmission electron microscopy (cryo-TEM) were performed on a JEOL JEM-2100 instrument operated at an acceleration voltage of 200 kV. Cryo-TEM specimens were prepared by applying a 4 μL drop of a dispersion sample to Lacey carbon-coated copper TEM grids (200 mesh, Science Services) and plunge-frozen into liquid ethane with an FEI Vitrobot Mark IV set at 4 °C and 95 % humidity. Vitrified grids were either transferred directly to the microscope cryogenic transfer holder (Gatan 914, Gatan, Munich, Germany) or stored in liquid nitrogen. Imaging was carried out at temperatures around 90 K. The TEM was operated at an acceleration voltage of 200 kV, and a defocus of the objective lens of about 2.5–3 μm was used to increase the contrast. Cryo-TEM micrographs were recorded at a number of magnifications with a bottom-mounted 4 k × 4 k CMOS camera (TemCam-F416, TVIPS, Gauting, Germany). The total electron dose in each micrograph was kept below 20 $e^-/Å^2$.

Small angle X-ray scattering (SAXS) and wide angle X-ray scattering (WAXS): SAXS/WAXS measurements of the PIL dispersions have been performed at the four crystal monochromator (FCM) beamline of the PTB at the BESSY II synchrotron radiation facility (Helmholtz-Zentrum Berlin, Germany).[56] The PIL dispersions have been measured in sealed 80.0 × 4.2 × 1.25 mm^3 borosilicate glass cuvettes purchased from Hilgenberg (Malsfeld, Germany, a wall thickness of *ca.* 120 μm). All measurements have been performed at a photon energy of (8000.0 ± 0.8) eV. The SAXS data have been recorded at a sample detector distance of (5.107 ± 0.005) m with a Pilatus 1 M detector (Dectris ltd., Baden, Switzerland) and a distance of (0.206 ± 0.002) m for WAXS measurement.[57] Distance from sample to detectors has been determined with the long-period spacing (001) peak of silver behenate by the triangulation method. To determine the scattering from the solvent and the glass-cuvettes, prior measurements of the empty cuvettes and pure water in a separate cuvette have been performed. In all measurements, the lower section of the cuvettes was filled with Fluorinert FC-3283 acquired from Iolitec (Heilbronn, Germany) to determine the optical path length of the cuvettes.[58] The SAXS and WAXS scattering images have been recorded on multiple spots along the cuvettes and averaged to reveal possible effects of sedimentation. The whole sequence of measurements was repeated three times to detect potential X-ray damage of the PIL NVs. The scattering images have been circularly averaged and the resulting SAXS data curves have been accordingly fitted using custom-made software with a model for hollow spherical core–shell particles under the assumption of a log-normal size distribution. The uncertainties of the fit parameters for the overall diameter and shell thickness and the errors of the fits of the SAXS data have finally been determined by the reduced χ^2- method.[59]

X-ray diffraction analysis (XRD): The powder XRD measurements were conducted on Bruker D8 using a monochromatized X-ray beam with Cu Kα radiation at a scan rate of 0.05°/min. The PIL/Cu samples were collected after freeze-drying and kept in an air-tight XRD holder from Bruker.

UV–vis absorption spectra: the colloidal dispersions of PILs and PIL/Cu composite samples were contained in a clean quartz cuvette (110-QS Hellma, 10 mm) and measured on a PerkinElmer Lambda 650 spectrometer at room temperature.

Thermogravimetric analysis (TGA): the fully dried PIL template and PIL/Cu composite samples were measured on PerkinElmer (TGA 8000) in a temperature range of 25–900 °C at a heating rate of 10 °C/min under synthetic air. The copper loading of PIL/Cu samples is calculated based on the mass of CuO residual after calcination in air.[53]

Quasi in situ X-ray photoelectron spectroscopy (XPS): the XPS measurements were carried out in a SPECS PHOIBOS 100 analyzer with Al Kα radiation (1486.74 eV). For the quasi *in situ* XPS measurements, the CO_2ER experiments were carried out in an O_2-free glovebox using the H-type cell specified above and under the same conditions. After the electrolysis, the samples were completely

dried and stored in the glovebox. The samples were then transferred to the XPS vacuum chamber using a transfer arm, which was kept under an inert atmosphere. Further details on the quasi *in situ* XPS measurements are referred to our previously published work.[60]

Coarse-grained simulations for self-assembled PIL NVs: The coarse-grained (CG) model for PILs is constructed with the following principles: the planar imidazolium ring is represented by a single bead carrying a partial charge of + 1.0 e; the Br^- anion is mapped into a single CG bead carrying a partial charge of −1.0 e; each ethyl or ethylene unit is coarsened into one neutral CG bead. The bonded and non-bonded interaction potentials between CG beads are described by the AMBER FF format. The effective interaction parameters between these CG beads were determined following the similar procedures described in the previous work.[61] In brief, the relative positions and sizes of these CG beads are determined from the center-of-mass of the corresponding atomistic units. The bonded interaction parameters between virtually bonded CG beads including bond stretching and angle bending terms were calibrated to reproduce probability distributions of bond lengths and angles of atomistic groups in ILs derived from extensive atomistic reference simulations. The non-bonded interaction parameters between CG beads were determined to reproduce microstructures (*e.g.*, radial distribution functions) of atomistic modeling systems at varied thermodynamic states.[61]

The CG MD simulations of the self-assembly behavior of PILs in an aqueous solution were performed using the GALAMOST package.[62] The equations of motion were integrated using a classical velocity Verlet leap-frog integration algorithm with a time step of 2.0 fs to accelerate CG MD simulations of PILs modelling systems at extended spatiotemporal scales with a modest computational cost. A cut-off distance of 1.6 nm was set for short-range *van der Waals* interactions and real-space electrostatic interactions between point charges. The ENUF method, an abbreviation for the Ewald summation based on the non-uniform fast Fourier transform technique, was employed to handle long-range electrostatic interactions in reciprocal space calculations.[63,64]

Each modeling system contains ∼375,000 CG beads and the number concentration of ion pair beads is kept at 20 %. The degree of polymerization (n) of PIL chains varies from 1 (IL monomer) to 50 to explore its overall effect on the self-assembled structures at constant C_m. Additional CG MD computations were performed for PILs consisting of 2, 4, 6, 12, and 30 IL monomers. All modeling systems were first energetically minimized using a steepest descent algorithm, and subsequently annealed gradually from 600 K to target temperatures within 10 ns. Afterwards, the system was equilibrated in an isothermal-isobaric ensemble for 20 ns of physical time maintained using Nose-Hoover thermostat and Parrinello-Rahman barostat with time coupling constants of 0.4 ps and 0.2 ps, respectively, to control temperatures and pressure at 1 atm. All CG MD simulations were sampled in a canonical ensemble for 20 ns, and simulation trajectories were recorded at an interval of 100 fs for further structural and dynamical analysis.

3. Results and discussion

3.1. Formation of PIL NVs via PISA

Polymerization induced self-assembly (PISA) of amphiphilic PIL homopolymers in an aqueous solution triggers the facile synthesis of well-defined PIL structures from a surfactant-like IL monomer. Without any externally added stabilizer in polymerization, stably dispersed PIL homopolymer particles in different forms were prepared in water, driven by incompatibility between the hydrophilic charged backbones and the hydrophobic neutral long alkyl substituents.[32] Herein, we began with the chemical synthesis of the amphiphilic IL monomer 3-*n*-decyl-l-vinylimidazolium bromide, followed by its free radical homopolymerization in an aqueous solution. The successful preparation of this monomer and its corresponding PIL (C_m at 12 mg/mL for initial tests) was confirmed by ^{1}H NMR measurements (see details in Fig. S1). Their thermal behavior and relative stabilities were subsequently characterized by DSC and TGA, as summarized in Fig. S2 and S3. A distinct melting peak at *ca.* 33 ℃ (below 100 ℃) for the IL monomers was observed in the DSC curve, which classifies itself into the group of ionic liquids. Besides, no apparent weight loss (up to 200 ℃) in its TGA curve was found for the as-synthesized PILs, indicating their good thermal stability (Fig. S3).

The self-assembly of the PIL can be controlled by simply polymerizing the IL monomer at chosen C_m. The morphologies of these featured PIL nanoparticles prepared at specific C_m in aqueous solution were first characterized by conventional TEM and SEM, as shown in Fig. S4 and S5, respectively. The samples for electron microscopies were prepared by drying their dispersions at room temperature. We observed that the particle size increased along with C_m from 3 to 6 mg/mL (Fig. S4). Subsequently, their shape was transformed from hollow NVs at $C_m \sim 12$ mg/mL, to dense spheres at $C_m \sim 24$ mg/mL, and finally into directional worms (at $C_m \sim 48$ mg/mL). Generally speaking, when polymerizing the IL monomer at both low (3 to 6 mg/mL) and medium C_m (from 6 to 12 mg/mL), the observed lighter contrast in the center area of PIL particles than their edge in TEM images indicates a hollow core that was filled with water before drying. The morphology of collapsed thin shells after drying under ambient conditions was similarly spotted in SEM images (Fig. S5). Interestingly, in the case of high C_m (from 12 to 24 mg/mL), the center void gradually shrank in size and eventually disappeared at $C_m \sim 24$ mg/mL or above to form only dense particles. A further increase of C_m to 48 mg/mL triggers the formation of linear PIL aggregates, *i.e.*, one-dimensional PIL fibers with a length of up to ∼ 10 μm and a diameter of (110 ± 13) nm. A similar morphology was observed in our previous report of a different PIL system.[65]

Due to the ambient-condition drying effect in the TEM sample preparation step, the authentic architecture, particularly the hollow inner structure of the PIL particles, is hard to be convincingly verified by conventional TEM. A morphology-verification step by cryo-TEM is thus required.[66] As shown in Fig. 1a-b, e-f, and S6, large spherical cavities inside PIL NVs were found at both low (3 to 6 mg/mL) and medium (6 to 12 mg/mL) C_m. In high C_m range (from 12 to 24 mg/mL), the ordered curved multilamellar wall gradually extended its thickness to downsize the central void (C_m at ∼ 16 mg/mL), and eventually filled in the hollow interior to form solid nanospheres (SNSs) at $C_m \sim 24$ mg/mL, as shown in Fig. 1c-d, and g-h. Beyond this concentration, *e.g.,* at $C_m \sim 48$ mg/mL, the linear attachment of primary PIL nanoparticles occurred and gave rise to hierarchical structures, namely primary nanoparticles formed first and next fused into nanoworms (Fig. 1i-k). For all PIL nanoparticles prepared in this work, a general molecular organization in the form of an alternating multilamellar packing of polymer chains was identified under the cryo-TEM conditions. The hydrophobic alkyl substituent as a side chain covalently tethered to the ionic polymer backbone accounts for the lighter lamellae domain in the cryo-TEM images, while the darker rings (or planes) stem from the polymer backbone made up of the imidazolium bromide ion pairs of a higher electron density.[65] The average bilayer spacing of NVs ($C_m \sim 12$ mg/mL) is measured to be (3.1 ± 0.1) nm from cryo-TEM images (see the detailed bilayer structure in Fig. S7).

By carefully analyzing the cryo-TEM images, we identify that the overall diameter and shell thickness of NVs (*i.e.,* the total thickness of the multilamellar layers shown in Fig. 2a) strongly depends on C_m in the polymerization. The particle sizes and size distribu-

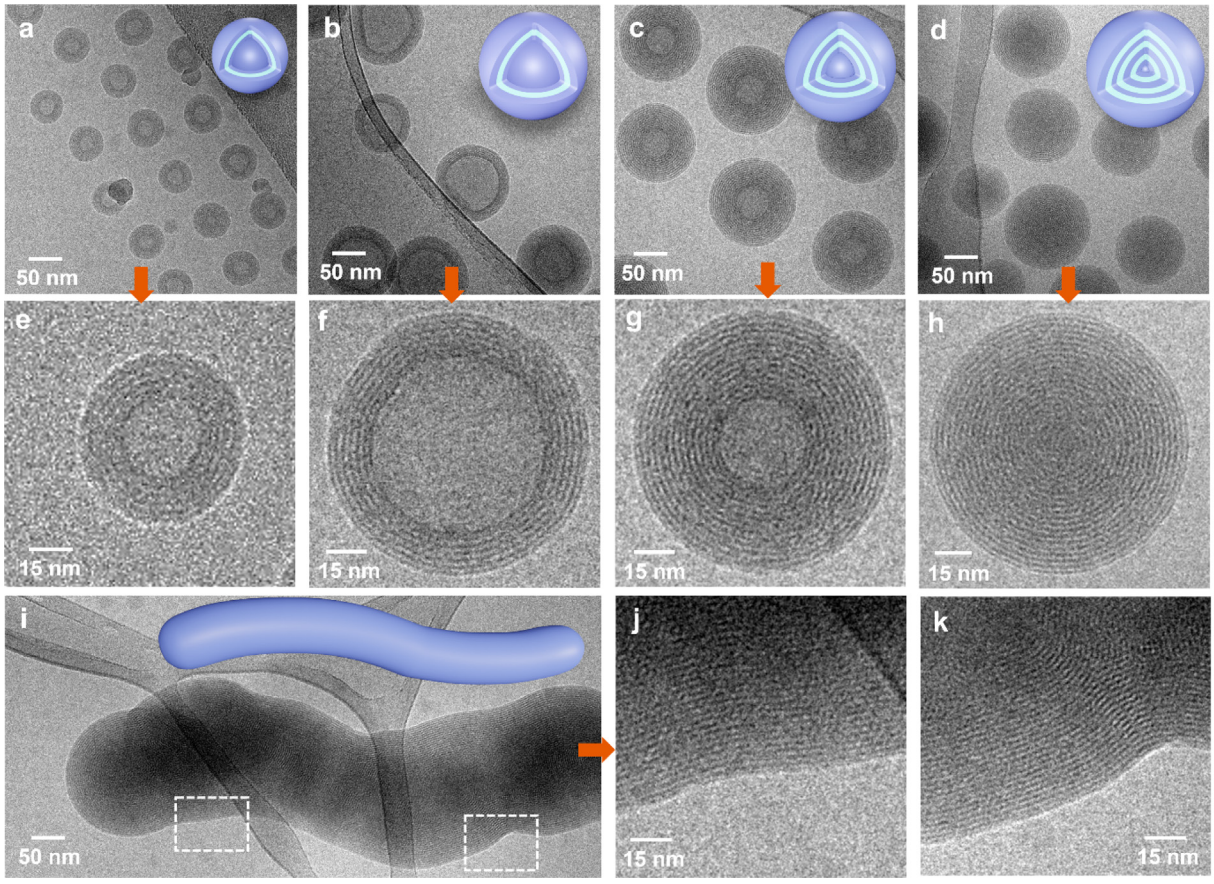

Fig. 1. Cryo-TEM images of the PIL NVs prepared *via* PISA method at various monomer concentrations (C_m): (a, e) 3 mg/mL, (b, f) 12 mg/mL, (c, g) 16 mg/mL, (d, h) 24 mg/mL, and (i-k) 48 mg/mL. The insets are the corresponding 3D models.

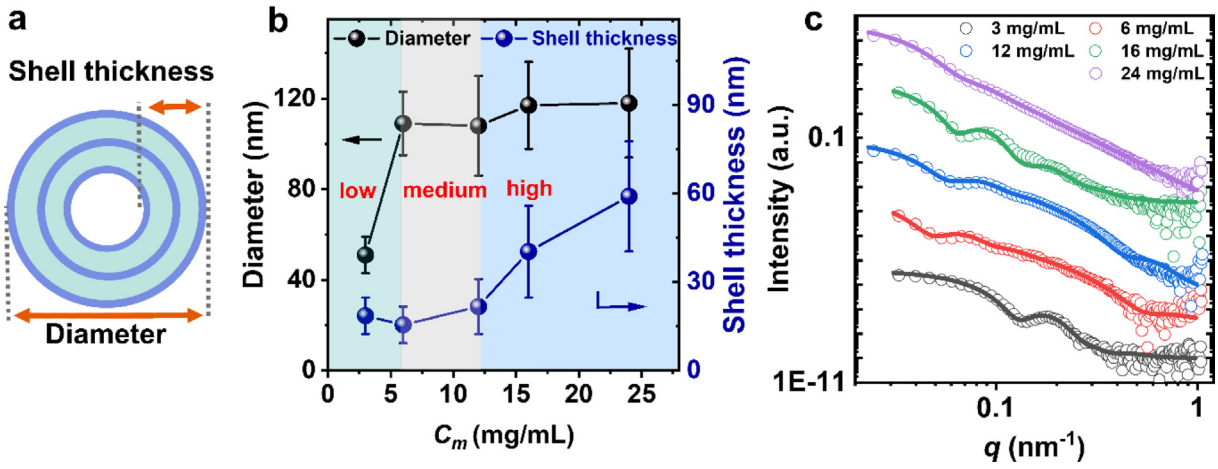

Fig. 2. (a) Scheme of the cross-section of the multilamellar PIL NVs. (b) Plots of the diameter and shell thickness of the PIL particles as a function of C_m. (c) SAXS profiles (scatter patterns) of the PIL dispersions prepared at various C_m plotted together with the analytical fit (solid lines) using a core–shell form factor. Scattering curves are vertically shifted for clarity.

tions determined from cryo-TEM analysis are shown in Fig. 2b and S8. Specifically, increasing C_m in the low range of 3 to 6 mg/mL leads to an initially dramatic expansion of the NVs size from (51 ± 8) to (109 ± 14) nm. In the medium C_m range (6 to 12 mg/mL), the diameter of PIL particles does not change significantly from (109 ± 14) to (108 ± 22) nm. Meanwhile at high C_m (12 to 24 mg/mL), the diameter increases slightly to (118 ± 28) nm at C_m ~ 24 mg/mL. It is worth noting that the shell thickness undergoes a slight decrease ranging from (18 ± 6) to (16 ± 6) nm in the low concentration zone (C_m of 3 to 6 mg/mL) and is followed by a minor jump to (22 ± 9) nm at medium C_m of 6 to 12 mg/mL. At higher C_m above 12 mg/mL till the C_m at which the hollow space is fully filled, the shell thickness sharply rises to a maximum value of (59 ± 14) nm. The D_h and distributions of these assembled nanoparticles were also determined by DLS and plotted against C_m (Fig. S9), and the results are in good agreement with cryo-

TEM analysis. Hence, it can be addressed that in the low C_m zone (below 6 mg/mL), the addition of more monomers only enlarges particle size. In the medium C_m zone (from 6 to 12 mg/mL), neither the particle size nor the shell thickness of PIL particles exhibits any drastic change. Polymerization at a high C_m (beyond 12 mg/mL) will vary the internal nanostructure by thickening the shell, triggering the complete transformation of NVs to SNSs (Fig. 1f-h and 2b). In short, the C_m is correlated with the shell thickness and the diameter of PIL NVs, which offers a useful tool to manipulate the dimension and morphology of PISA-induced PIL homopolymer nanostructure.

To verify the structural information, the colloidal dispersions of the PIL particles were further investigated by synchrotron-based SAXS/WAXS measurements. Fig. 2c displays their corresponding SAXS profiles at various C_m. Taking PIL NVs prepared at C_m-$\sim$ 3 mg/mL as an example, their SAXS plot has been fitted in the region from 0.04 to 0.8 nm^{-1} with an analytical form factor of a core–shell particle F_{cs} according to the following equation (2):

$$F_{CS}(q,R,v) = F_{Sphere}(q,\ R) - (1-\mu)F_{Sphere}(q, v\cdot R) \quad (2)$$

where F_{Sphere} $(q,\ R)$ is the form factor of a sphere with an overall radius R, q is the scattering vector, μ is the electron density difference between core and solvent relative to the shell contrast, and v is the ratio of the core radius to R.[67] To simplify the model, the PIL vesicle is assumed to logically adopt a hollow core (μ = 0) filled with water as a solvent. Moreover, a homogeneous shell is assumed here and the scattering from the internal lamellar layers is not considered in the simplified form factor of the fit.[68] The particle size distribution is further given in the form of a log-normal distribution. The fit of the SAXS profile reveals an average diameter of (56.1 ± 3.8) nm with a size distribution of *ca.* 7.9 nm, which resembles the results of cryo-TEM at (51 ± 8) nm. The shell thickness is determined to be (16.0 ± 2.2) nm, which also agrees well with that of cryo-TEM. The overall diameter and shell thickness of all the PIL particles were summarized in Table S1, generally following a similar trend to that of cryo-TEM analysis. In addition, the prominent peak is located at a q value of *ca.* 2.1 nm^{-1} in the WAXS data originated from the bilayer spacing of the NVs (Fig. S10). The average bilayer spacing is calculated to be (3.0 ± 0.1) nm based on Bragg's law, which is in good accordance with the value of (3.1 ± 0.1) nm determined in the cryo-TEM analysis.[69] The bilayer spacing of all the PIL assemblies shows only a slightly different value of 2.9 to 3.1 nm, confirming that the bilayer spacing stays constant, independent on the final morphologies of the assembled PIL NVs (Table S2).

3.2. Evolution mechanism of PIL NVs

Generally speaking, the morphology transformation and structural characteristics of polymer vesicles strongly correlate with the chain structure and polymer concentration.[9,70,71] In the current study, a higher C_m indicates a higher polymer concentration (see Table S3). At a low C_m window ranging from 3 to 6 mg/mL, we found a sharp increase in overall diameter but little change in thickness (Fig. 2b). Before polymerization, the 1-vinylimidazolium cations in IL monomer in water are reported to be associated with counter anions *via* Coulombic interaction.[72] The subsequent polymerization leads to the spontaneous self-organization of PIL chains packing into layered assemblies (as primary particles) due to the strong hydrophobic interaction of the long alkyl groups.[65] Meanwhile, the propagating PIL chains can be diffusively captured by the primary PIL vesicles until all the IL monomers are depleted. In addition, the primary particles tend to coalesce together and eventually form stabilized particles. Both effects could contribute to the appreciable size expansion of PIL vesicles when increasing C_m. In the medium C_m zone (from 6 to 12 mg/mL), however, neither the diameter nor the shell thickness of the PIL vesicles shows the drastic change. A possible explanation is that the number of the PIL particles increased due to the enhanced polymer concentration.[9]

At an even high C_m (from 12 to 24 mg/mL), we observed only a significant increase in shell thickness but a slight change in ultimate diameter. Particle coalescence or diffusion capture of PIL chains could not fully explain the increase in the shell thickness rather than diameter. It is essential to gain a deeper insight into the structural evolution in a molecular chain level. Chain length of amphiphilic homopolymers has been reported to affect their final assembly morphologies.[73,74] GPC (see Fig. S11 and Table S4) was thereby used to determine the number-averaged molecular weight (M_n) of PIL chains. Elevating C_m from 12 to 24 mg/mL increases their M_n from 43 to 49 kg/mol. Note that the M_n reported here stands for an apparent molecular weight using polystyrene standard for lack of suitable PIL standards, which can sufficiently reflect the relative length of PIL chains. When keeping the initiator concentration constant, a high C_m in free radical homopolymerization leads to a high propagating rate and therefore the formation of long PIL chains.[75] As a result, the PIL chain length (or M_n) is suggested to play a dominant role in the internal organization at high C_m, which will be further discussed in the latter simulation part. In principle, the increase in shell thickness could be separately or simultaneously realized in two possible ways: one mainly results from the expansion of the bilayers, which is commonly found in block copolymers; [76,77] the other primarily comes from the folding of more bilayers into the vesicle center. Evidently, the shell thickening of our PIL homopolymer NVs will merely expand in the latter manner. Independent on the C_m, the bilayer spacing keeps practically constant for all PIL NVs, which has been proved by cryo-TEM and WAXS analyses (Table S2). When the C_m keeps increasing (up to 48 mg/mL), the strong Hamaker force induced by charge polarization promotes the alignment organization of the neighboring particles due to the liquid character of their interior. Thus, the PIL particles partially deform and fuse into directional worms, as described in our previous study.[65]

Extensive coarse-grained (CG) molecular dynamics simulations were performed to confirm the dependence of self-assembled structures of PILs on the polymerization degree (n), *i.e.*, chain length of PILs. The adopted CG model for the IL monomer cation 3-*n*-decyl-l-vinylimidazolium is depicted in Fig. 3a. The principles for constructing such a CG model and determining the effective interaction potentials between CG beads were detailed in our previous work.[61] The relevant computational methodology is provided in Supporting Information. On account of the high bending energy, short PIL chains will require a long time to mediate their spatial distributions and coordinate with anions and solvent molecules.[78] In comparison to neutral polymers, our cationic PILs by virtue of their ionic nature present a more complex molecular organization behavior. For polyelectrolytes, the electrostatic interactions between and inside polymer chains have been documented to result in counterion condensation.[79,80] The number of condensed counterions increases with the polymerization degree and polymer concentration. The strong condensation effect is likely to weaken the intrachain repulsion, thus driving severe deformation of polymer chains (mostly shrunk, collapsed, or unfolded chains).[81,82] In our case, as the presence of long side chains attached to the PIL backbone provides a strong steric hindrance between the neighboring PIL chains; it could favor retaining their layered packing rather than complete collapse during assembly. Therefore, the interplay of the effects as mentioned above presumably jointly facilitates the formation of well-defined vesicular nanostructures with anions and solvent molecules encapsulated inside (Fig. 3b and 3c).

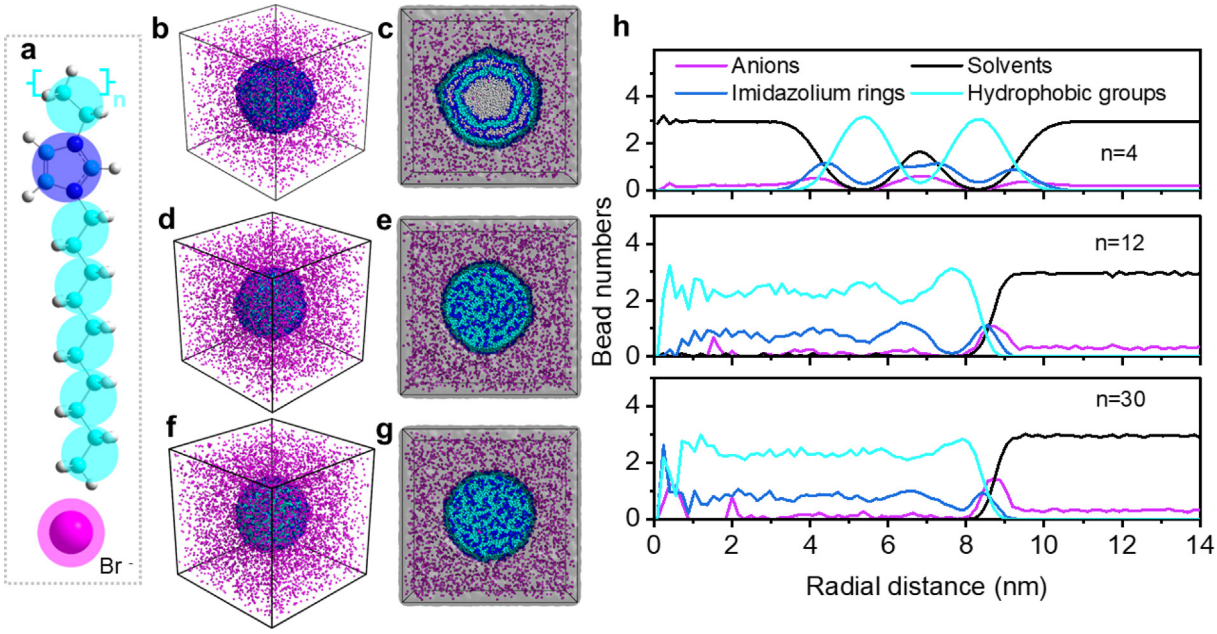

Fig. 3. (a) The constructed CG model for 3-*n*-decyl-1-vinylimidazolium bromide. Full and cross-section views of the self-assembled structure of PILs in an aqueous solution. PIL (b, c) with $n = 4$, (d, e) $n = 12$, and (f, g) $n = 30$. The solvent molecules encapsulated within and outside the self-assembled PIL particles are indicated by a gray medium. (h) Number density distributions of the CG beads in PILs, anions, and solvent molecules in modeling systems.

It is noticeable that a gradual increase in chain length from monomeric to an oligomeric chain with 6 repeating units (*i.e.*, n of 1 to 6) promotes a considerable expansion of the inner space of vesicular structures, and thereafter a substantial decrease in the inner volume with a further lengthening of PIL chains (Fig. S12). It resembles the experimental results of PIL NVs with the C_m increasing from 3 to 6 mg/mL. PILs with intermediate chain length (n = 12 in Fig. 3d and 3e) are self-assembled into solid spheres with residual solvent molecules incorporated inside, which is in line with the transformation of PIL NVs to SNSs (C_m of 12 to 24 mg/mL). PILs with an even longer chain (n = 30 in Fig. 3f and 3 g) tend to form solid self-assembled structures with less solvent encapsulated than the PIL NVs. On the basis of these findings, we may argue that the PIL chains with relatively higher n are more likely to extend into the center of the vesicle due to their better flexibilities and weaker intrachain repulsions, thus diminishing the central cavity. The number density distributions of representative CG beads in modeling systems (Fig. 3h) demonstrate that the self-assembled structures from PILs with intermediate and long backbones are characterized by structure-less interior and stripe-patterned shells, which are probably relevant to the residual solvent molecules inside the self-assembled PIL particles. Therefore, we demonstrated that the polymerization degree of PIL homopolymers plays an essential role in dictating the overall shell thickness (*i.e.*, the number of folded bilayers), thus enabling the transformation of their morphology.

3.3. PIL NVs-supported ultra-small CuNPs for CO_2ER

PIL NVs were further explored as a template to immobilize and stabilize ultra-small CuNPs. The obtained PIL/Cu composite particles were utilized as electrocatalysts for CO_2ER. Briefly, the PIL templates were incubated with $CuAc_2$ salt in an aqueous solution for 4 h to ensure sufficient enrichment of the Cu^{2+} ions into the PIL particles. Subsequently, the copper ions were reduced into metallic copper in the presence of N_2H_4 as a strong reducing agent at 80 °C (Fig. 4a).[53] As a result, ultra-small CuNPs (highlighted by white arrows in Fig. 4b) were directly immobilized into the PIL nanostructures. In addition, the multilamellar structure in PIL NVs was observed to be slightly distorted in the composite particles. While N_2H_4 treatment can hardly influence the morphology of PIL NVs (Fig. S13), penetration of Cu^{2+} ions into the neighboring PIL layers is likely the drive for deforming the PIL internal structure. The CuNPs in NVs (denoted as NVs/Cu thereafter) and in SNSs (denoted as SNSs/Cu thereafter) show an average particle size of (1.8 ± 0.4) and (1.7 ± 0.5) nm, respectively (Fig. 4c and S14). The successful incorporation of CuNPs within the PIL templates is supported by the observation of a weak absorption peak at 200 to 300 nm in the UV–vis absorption spectra (Fig. 4d).[49] To confirm the presence of CuNPs, the PIL/Cu composite particles and the pristine PIL templates were characterized by X-ray diffraction (XRD). As shown in Fig. 3e, three distinct peaks at 43°, 55°, and 74° are observed for both PIL/Cu composite particles, which can be assigned to the (111), (200), and (220) reflections of face-centered cubic (*fcc*) metallic Cu, respectively. The pure PIL templates show no reflection at all due to their amorphous nature, which is in line with the DSC analysis (Fig. S2). The amount of copper loading in PIL NVs/Cu and SNSs/Cu is 19.2 and 8.9 wt%, respectively, calculated from the aerobic residual (CuO) in the TGA test (Fig. 4f and S15). The PIL NVs show a higher Cu loading than that of SNSs, as expected for a hollow structure with a relatively higher specific surface area (Fig. S16) to provide more surface area to load CuNPs as active sites for CO_2ER. As reference, pristine CuNPs were prepared using the same protocol but without any PIL template. Only Cu particles with an irregular morphology were obtained. Their much larger size was revealed by SEM and TEM images (Fig. S17), emphasizing the essential role of PIL NVs in controlling the ultra-small size of CuNPs in the composite particles.

The as-prepared pristine CuNPs and NVs/Cu particles were directly spray-coated on GDLs. The coated GDLs were served as the working electrode for CO_2ER experiments (Fig. 5a). The CO_2ER activity was examined in a CO_2-saturated 0.1 M $KHCO_3$ solution using a conventional H-cell configuration (Fig. S18). The product distributions (Faradaic efficiency, FE) of the CO_2ER as a function of the applied potential of the synthesized catalyst materials are summarized in Fig. 5b and S19. At low negative potentials between

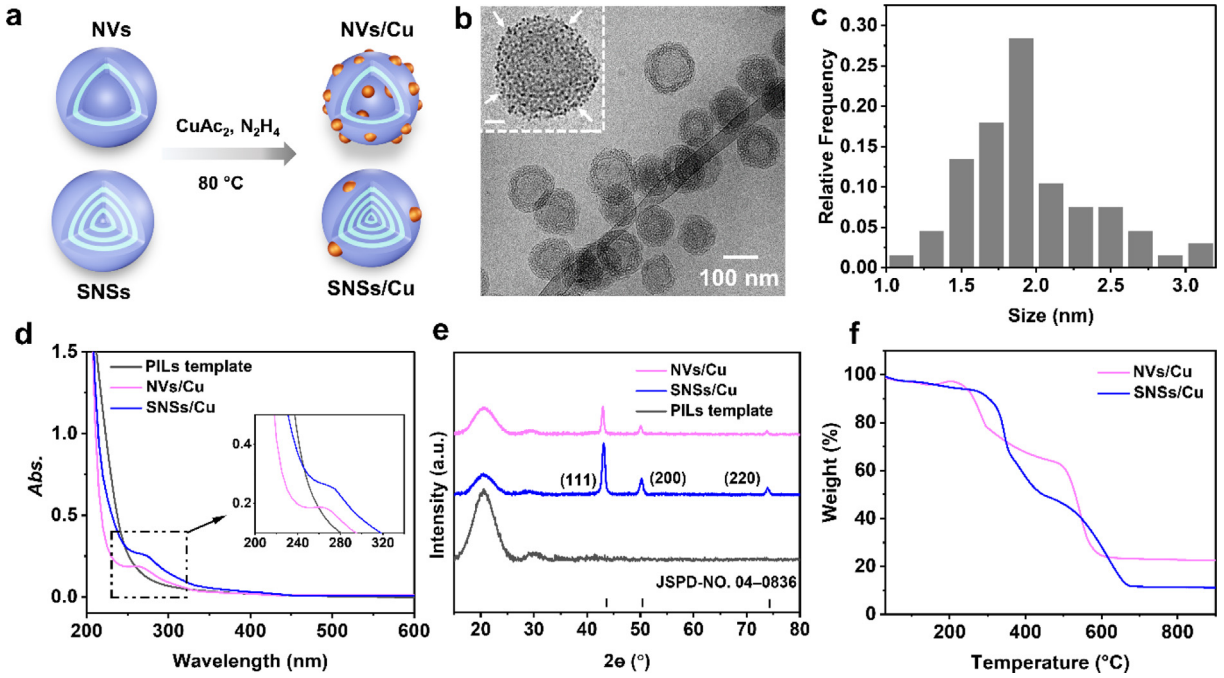

Fig. 4. (a) Scheme of the synthesis of the colloidal PIL/Cu composite particles. (b) Cryo-TEM images of the PIL NVs/Cu composite particles. The inset is a close view with a scale bar of 30 nm and some tiny CuNPs are indicated by white arrows. (c) The corresponding size distribution histogram of CuNPs (calculated from over 100 particles) in PIL NVs/Cu determined from its cryo-TEM image. (d) UV–vis absorption spectra of the dispersions of PIL template, NVs/Cu, and SNSs/Cu. (e) XRD diagrams of the PIL templates, NVs/Cu, and SNSs/Cu powders after a thorough freeze-dry, which are referenced to the JSPD card (Cu: 04–0836). (f) TGA curves measured under synthetic air of the NVs/Cu and SNSs/Cu powder after freeze-drying.

−0.8 and −0.9 V *vs* RHE, a mixture of H_2 and C_1 products (CO, CH_4, and $HCOO^-$) were the major products in the case of all studied electrocatalysts. For the PIL NVs/Cu electrodes, with the applied potential increasing from −0.8 to −1.1 V the total FE of all C_1 products increased from ∼ 38 % to ∼ 58 %, concurring with decreasing H_2 FE. It is notable that the FE of CH_4 significantly increased from ∼ 6 % to ∼ 34 % when the potential increased from −0.8 to −1.2 V for NVs/Cu, while the FE of CH_4 of the pristine CuNPs remained below 8 % (Fig. 5b). Upon increasing the applied cathodic bias, the FE of the pristine CuNPs shifts from C_1 products (CO and $HCOO^-$ as main products) towards C_2/C_{2+} products (mainly C_2H_4), see Fig. S19. In other words, the FE of the pristine CuNPs entirely shifts to C_{2+} products at the expense of C_1 products, while the FE of the PIL NVs/Cu shifts from CO and $HCOO^-$ to CH_4 as a major product (Fig. 5b and S19). Note that the PIL SNSs/Cu shows higher selectivity towards H_2 generation despite having similar CH_4 selectivity to that of NVs/Cu (Fig. S20). Thus, we focused on PIL NVs/Cu for further study. Overall, our PIL/Cu composite particles show relatively high CH_4 selectivity compared with the current reports, as shown in Table S5.

To gain deep insights into the CO_2ER behavior of the pristine CuNPs and PIL NVs/Cu, the partial current densities (*i.e.*, production rates) of their main products are displayed in Fig. 5c and d. An increase in H_2 production was observed for both catalysts upon increasing the applied cathodic potential. The PIL NVs/Cu showed a significant surge in CH_4 production rate from ∼ 2.0 to 38 mA mg^{-1} cm^{-2} when the applied cathodic potential increased from −0.9 to −1.2 V. As shown in Fig. S21, the PIL NVs/Cu also exhibited higher specific current density than the commercial CuNPs (40–60 nm in size). Additionally, the FE ratio of CH_4/C_2H_4 on PIL NVs/Cu particles was enhanced by a factor of 22 at −1.2 V in comparison with that of pristine CuNPs, highlighting the significant impacts of PIL templates on the CuNPs electrocatalytic behavior for CO_2ER.

Apart from the structural merits of the hollow nanovesicle, the chemical nature of PIL NVs is expected to crucially facilitate the CO_2ER process. The enhanced selectivity of CO_2ER towards CH_4 on NVs/Cu could be attributed to one (or more) of the following effects: (1) special surface defects (low coordinated sites) provided by the small size of CuNPs in PILs; (2) stabilizing effect of key intermediates for CH_4 by surface functionalities of PILs; (3) electronic interactions between the PILs and the CuNPs. It has been reported in recent works that a strong interfacial electric field induced by the imidazolium moieties at the PIL/Cu interface could stabilize key intermediates in CO_2ER.[47,83] Quasi *in situ* XPS was employed here to investigate the interplay between the CuNPs and PILs, and to examine the induced surface speciation changes of PIL/Cu induced during CO_2ER. The results are displayed in Fig. 6 and Fig. S22. As-prepared pristine CuNPs (in the absence of PILs) showed a mixture of Cu^{2+}, which is indicated by the observed shoulder peak at 934.2 eV, and Cu^+/Cu^0 as demonstrated by the strong sharp peak at 932.3 eV. On the other hand, the as-synthesized PIL NVs/Cu exhibited merely a single peak at 936.0 eV, which is strongly shifted to higher binding energy than the observed Cu^{2+} peak of the pristine CuNPs (see Fig. 6a and c). This may suggest an intense electronic interaction between Cu and the polyimidazolium backbone *via* the formation of copper 1,3-dialkylimidazol-2 ylidene carbene complex, which is different from the copper oxide species (*e.g.*, CuO and $Cu(OH)_2$).[49,84] The absence of the metallic Cu surface species in the case of pristine CuNPs was further indicated by fitting the Auger region, see Fig. 6d. Following the application of the cathodic bias, both the pristine CuNPs and the NVs/Cu exclusively exhibited metallic Cu surface species, as indicated by the absence of the Cu^{2+} shoulder and its related strong satellite on the Cu 2p spectra. The full reduction of the oxidized copper surface species of both electrodes (pristine CuNPs and NVs/Cu) during CO_2ER is further indicated by their respective fitted Auger regions (Fig. 6b and d). The post XPS surface analysis of the NVs/Cu catalyst after CO_2ER (air-exposed) shows a surface consisting of a mixture of Cu^{2+} and Cu^+ species resembling the as-prepared pristine CuNPs. The related peaks for the Cu^{2+} and

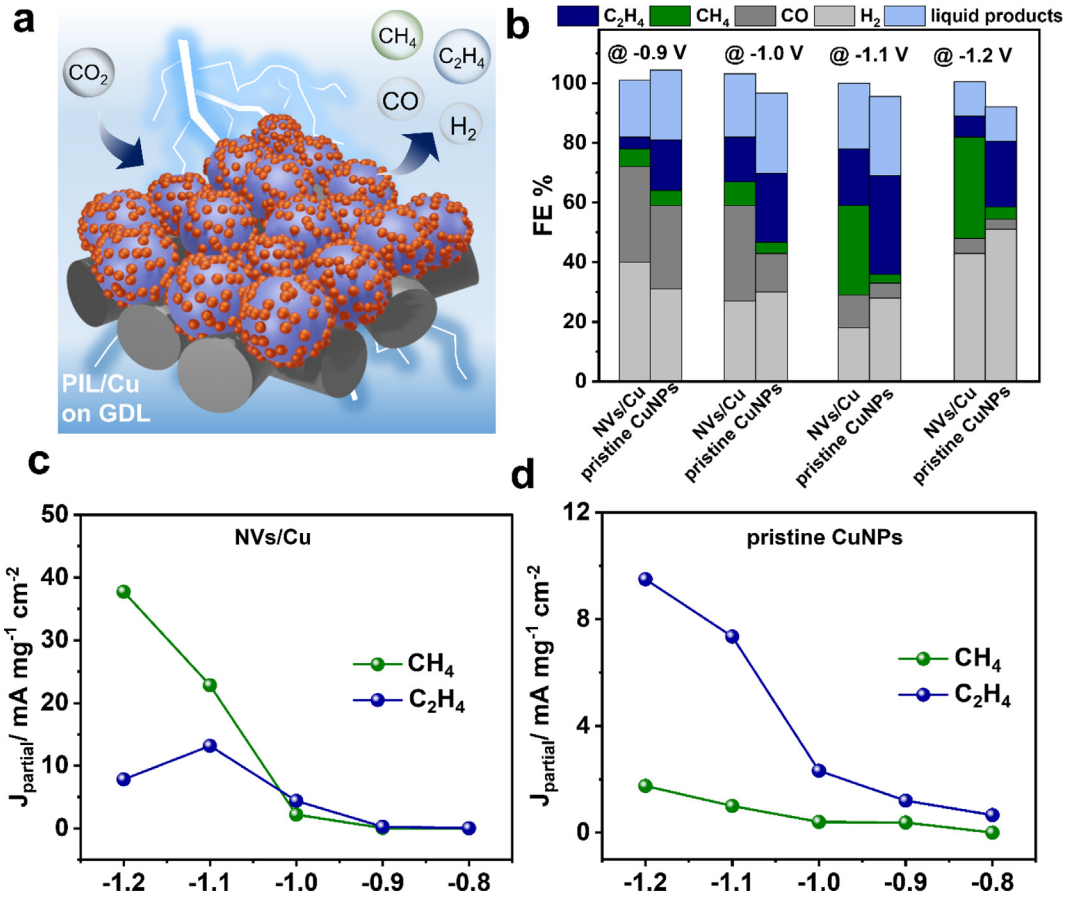

Fig. 5. (a) Scheme of CO_2ER using PIL/Cu composite particles after coating on GDLs. (b) Summary of the CO_2ER activity trend for various catalysts, highlighting the tunable selectivity toward CH_4. The complete dataset is found in Fig. S19. FE% of the PIL NVs/Cu and pristine CuNPs coated GDLs is measured in CO_2-saturated 0.1 M $KHCO_3$ solution at applied potentials (V *vs* RHE). Partial current density toward the generation of CH_4 and C_2H_4 on (c) NVs/Cu, (d) pristine CuNPs as a function of applied potential.

Cu^+ surface species were observed at 932.5 eV and 934.6 eV, respectively, which are still positively shifted (~0.2 eV) compared to that of the pristine CuNPs. The appearance of the mixture of Cu^+ and Cu^{2+} for the PIL/Cu catalysts after CO_2ER instead of the strong positively shifted peak may indicate the transformation of the PILs under CO_2ER measuring conditions. The transformation of PILs under bias was also evidenced by the observed significant changes in the obtained C 1 s spectra of PIL NVs/Cu before and after CO_2ER, see Fig. S22. Regardless, retesting the same electrode after removal of bias in a fresh electrolyte still showed a high FE towards CH_4 (33 % FE). Based on these XPS results, the enhanced C_1 selectivity of the PIL NVs/Cu electrode might be attributable to the strong electronic interaction between PILs and CuNPs as well as the ultra-small size of CuNPs, resulting from *in situ* reduction of PIL NVs/Cu complex under CO_2 electrolysis conditions. The enhanced CH_4 production due to the reduction of Cu from copper complexes is also in line with previous findings.[85,86]

4. Conclusion

In summary, we successfully fabricated PIL homopolymer NVs with a characteristic multilamellar chain stacking *via* free radical homopolymerization, which is in line with our previous studies. [30,52] Their morphologies were tailored from hollow to solid spheres, further to directional solid worms by simply increasing C_m applied in polymerization. Manipulation of the overall size and shell thickness of PIL NVs has been achieved by tuning the C_m, which has been scarcely reported before. Next, we systematically studied the influence of the C_m on their size variation and morphological transformation. The formation mechanism of PIL NVs has been further confirmed by CG simulations, illustrating the essential role of polymerization degree of PIL chains in directing the assembly behavior. Our well-defined PIL NVs with a hollow interior enabled high loading amounts of ultra-small CuNPs (1–3 nm in size) that were used for CO_2ER. Large pristine CuNPs and PIL-functionalized CuNPs (above 30 nm) have been reported to improve the selectivity towards C_2 products in CO_2ER. [47,83] In our study, PIL/Cu composite particles exhibited a high FE towards C_1 products, especially CH_4 (FE of ~ 34 % at −1.2 V). The XPS analysis showed that the strong electronic interactions between the imidazolium units of PILs and the surface Cu atoms of CuNPs results in the high FE towards CH_4. This contribution highlights the potential of future research interest in the use of well-defined PILs to tune the selectivity of metallic electrocatalysts for CO_2 reduction. Future work is expected to deepen our understanding *via* a systematic study on the role of PIL and the size effect of CuNPs on CO_2ER performance by *in situ* Raman and XPS.

CRediT authorship contribution statement

Xuefeng Pan: Conceptualization, Writing – original draft. **Zdravko Kochovski:** Resources, Software. **Yong-Lei Wang:** Methodology, Visualization, Software. **Radwan M. Sarhan:** Investigation, Validation. **Eneli Härk:** Resources, Data curation. **Siddharth Gupta:** Investigation, Validation. **Sasho Stojkovikj:** Validation, Resources. **Gumaa A. El-Nagar:** Formal analysis, Writing – review

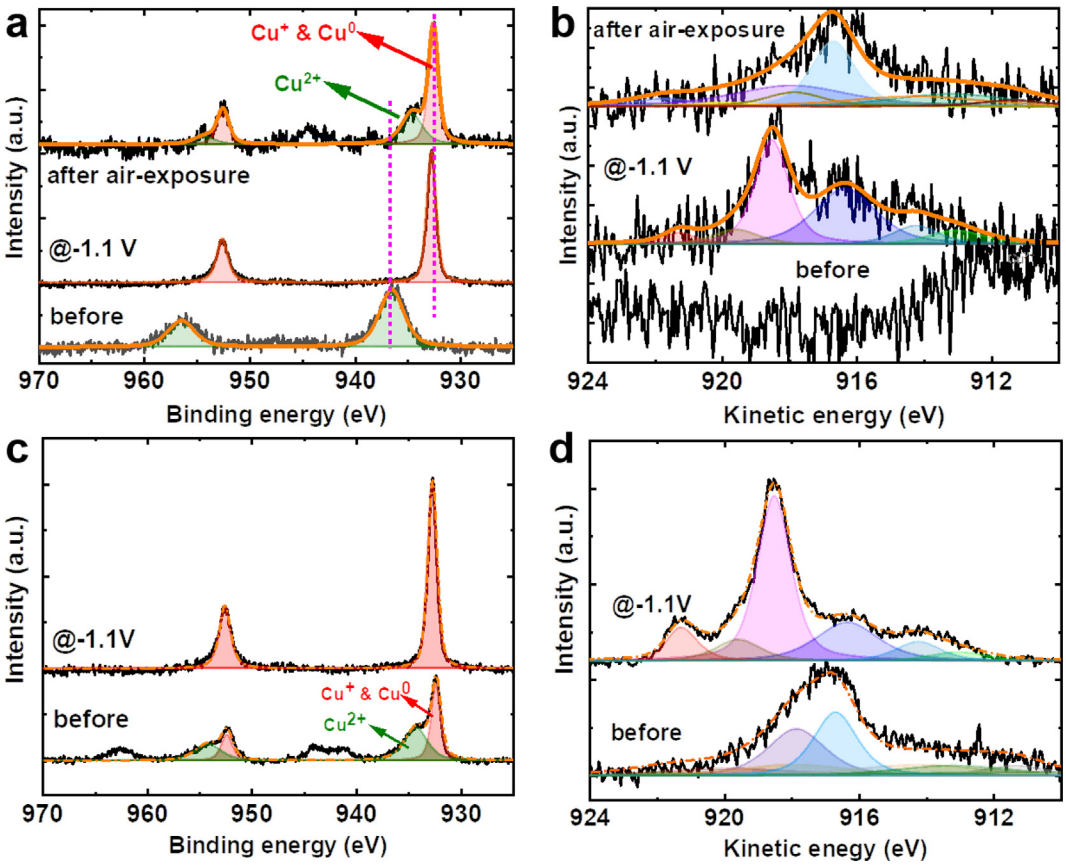

Fig. 6. Quasi *in situ* XPS results of (a, b) the NVs/Cu and (c, d) the pristine CuNPs: (a, c) the Cu 2p XPS spectra and (b, d) the respective Cu Auger regions.

& editing. **Matthew T. Mayer:** Funding acquisition, Writing – review & editing. **Robin Schürmann:** Visualization, Methodology. **Jérôme Deumer:** Resources, Data curation. **Christian Gollwitzer:** Validation, Writing – review & editing. **Jiayin Yuan:** Supervision, Writing – review & editing. **Yan Lu:** Project administration, Supervision, Funding acquisition, Writing – review & editing.

Data availability

Data will be made available on request.

Declaration of Competing Interest

The authors declare that they have no known competing financial interests or personal relationships that could have appeared to influence the work reported in this paper.

Acknowledgements

The authors thank Flora Haun from Freie Universität Berlin for the great help in electrochemical experiments. The authors also thank Ms. Qiong Fang and Yi Chen for the suggestions in 3D modelling. Y. L. also thanks the Deutsche Forschungsgemeinschaft (DFG, German Research Foundation) - Project number 410871749 for financial support. The authors also thank the Joint Lab for Structural Research at the Integrative Research Institute for the Sciences (IRIS Adlershof) for cryo-TEM measurements. J. Y. appreciates the financial support of the Knut and Alice Wallenberg Foundation under the program Wallenberg Academy Fellow (WAF2017.0166) and the European research council consolidator grant (PARIS-101043485), and computations were performed using computational resources provided by Swedish National Infrastructure for Computing (SNIC) at PDC, HPC2N, and NSC partially funded by Swedish Research Council through grant agreement no. 2016-07213. This work was supported in part by the Helmholtz Association's Initiative and Networking Fund (Helmholtz Young Investigator Group VH-NG-1225) and the European Union's Horizon 2020 research and innovation program project FlowPhotoChem (grant agreement 862453). The material presented and views expressed here are the responsibilities of the author (s) only; the EU Commission takes no responsibility for any use made of the information set out.

Appendix A. Supplementary data

Supplementary data to this article can be found online at https://doi.org/10.1016/j.jcis.2023.01.097.

References

[1] R.M. Gorgoll, K. Harano, E. Nakamura, Nanoscale Control of Polymer Assembly on a Synthetic Catalyst-Bilayer System, J. Am. Chem. Soc. 138 (30) (2016) 9675–9681.
[2] A. Joseph, C. Contini, D. Cecchin, S. Nyberg, L. Ruiz-Perez, J. Gaitzsch, G. Fullstone, X. Tian, J. Azizi, J. Preston, G. Volpe, G. Battaglia, Chemotactic synthetic vesicles: Design and applications in blood-brain barrier crossing, Sci. Adv. 3 (8) (2017) e1700362.
[3] Y. Zhu, L. Fan, B. Yang, J. Du, Multifunctional Homopolymer Vesicles for Facile Immobilization of Gold Nanoparticles and Effective Water Remediation, ACS Nano 8 (5) (2014) 5022–5031.
[4] P. Tanner, P. Baumann, R. Enea, O. Onaca, C. Palivan, W. Meier, Polymeric Vesicles: From Drug Carriers to Nanoreactors and Artificial Organelles, Acc. Chem. Res. 44 (10) (2011) 1039–1049.
[5] M. Fauquignon, E. Courtecuisse, R. Josselin, A. Mutschler, A. Brûlet, M. Schmutz, J.-F. Le Meins, Large hybrid Polymer/Lipid Unilamellar vesicle (LHUV) at the

nanoscale: An insight into the lipid distribution in the membrane and permeability control, J. Colloid Interface Sci. 604 (2021) 575–583.
[6] Y. Zhu, B. Yang, S. Chen, J. Du, Polymer vesicles: Mechanism, preparation, application, and responsive behavior, Prog. Polym. Sci. 64 (2017) 1–22.
[7] M. Sasidharan, K. Nakashima, Core–Shell–Corona Polymeric Micelles as a Versatile Template for Synthesis of Inorganic Hollow Nanospheres, Acc. Chem. Res. 47 (1) (2014) 157–167.
[8] R.A. Ramli, Hollow polymer particles: a review, RSC Adv. 7 (83) (2017) 52632–52650.
[9] T. Nishimura, S. Shishi, Y. Sasaki, K. Akiyoshi, Thermoresponsive Polysaccharide Graft Polymer Vesicles with Tunable Size and Structural Memory, J. Am. Chem. Soc. 142 (27) (2020) 11784–11790.
[10] Q. He, D.-H. Tuo, Y.-F. Ao, Q.-Q. Wang, D.-X. Wang, Vesicles Constructed with Chiral Amphiphilic Oxacalix[2]arene[2]triazine Derivatives for Enantioselective Recognition of Organic Anions, ACS App. Mater. Interfaces 10 (4) (2018) 3181–3185.
[11] W. Jiang, Y. Zhou, D. Yan, Hyperbranched polymer vesicles: from self-assembly, characterization, mechanisms, and properties to applications, Chem. Soc. Rev. 44 (12) (2015) 3874–3889.
[12] D. Gaur, N.C. Dubey, B.P. Tripathi, Biocatalytic self-assembled synthetic vesicles and coacervates: From single compartment to artificial cells, Adv. Colloid Interface Sci. 299 (2022) 102566.
[13] Q. Chen, H. Schönherr, G.J. Vancso, Block-Copolymer Vesicles as Nanoreactors for Enzymatic Reactions, Small 5 (12) (2009) 1436–1445.
[14] C.K. Wong, A.D. Martin, M. Floetenmeyer, R.G. Parton, M.H. Stenzel, P. Thordarson, Faceted polymersomes: a sphere-to-polyhedron shape transformation, Chem. Sci. 10 (9) (2019) 2725–2731.
[15] S. So, T.P. Lodge, Size Control and Fractionation of Ionic Liquid Filled Polymersomes with Glassy and Rubbery Bilayer Membranes, Langmuir 32 (19) (2016) 4959–4968.
[16] J. He, L. Wang, Z. Wei, Y. Yang, C. Wang, X. Han, Z. Nie, Vesicular Self-Assembly of Colloidal Amphiphiles in Microfluidics, ACS App. Mater. Interfaces 5 (19) (2013) 9746–9751.
[17] J.R. Howse, R.A.L. Jones, G. Battaglia, R.E. Ducker, G.J. Leggett, A.J. Ryan, Templated formation of giant polymer vesicles with controlled size distributions, Nat. Mater. 8 (6) (2009) 507–511.
[18] C. Lebleu, L. Rodrigues, J.-M. Guigner, A. Brûlet, E. Garanger, S. Lecommandoux, Self-Assembly of PEG-b-PTMC Copolymers: Micelles and Polymersomes Size Control, Langmuir 35 (41) (2019) 13364–13374.
[19] L. Ma, A. Eisenberg, Relationship between Wall Thickness and Size in Block Copolymer Vesicles, Langmuir 25 (24) (2009) 13730–13736.
[20] J. Yuan, M. Antonietti, Poly(ionic liquid)s: Polymers expanding classical property profiles, Polymer 52 (7) (2011) 1469–1482.
[21] J. Yuan, D. Mecerreyes, M. Antonietti, Poly(ionic liquid)s: An update, Prog. Polym. Sci. 38 (7) (2013) 1009–1036.
[22] S.-Y. Zhang, H. Miao, H.-M. Zhang, J.-H. Zhou, Q. Zhuang, Y.-J. Zeng, Z. Gao, J. Yuan, J.-K. Sun, Accelerating Crystallization of Open Organic Materials by Poly (ionic liquid)s, Angew. Chem. Int. Ed. 59 (49) (2020) 22109–22116.
[23] J.-K. Sun, Y.I. Sobolev, W. Zhang, Q. Zhuang, B.A. Grzybowski, Enhancing crystal growth using polyelectrolyte solutions and shear flow, Nature 579 (7797) (2020) 73–79.
[24] D. Xie, Y. Xu, Y. Wang, X. Pan, E. Härk, Z. Kochovski, A. Eljarrat, J. Müller, C.T. Koch, J. Yuan, Y. Lu, Poly(ionic liquid) Nanovesicle-Templated Carbon Nanocapsules Functionalized with Uniform Iron Nitride Nanoparticles as Catalytic Sulfur Host for Li–S Batteries, ACS Nano 16 (7) (2022) 10554–10565.
[25] Y. Jiang, D. Li, Y. Zhao, J. Sun, Hydrogen bond donor functionalized poly(ionic liquids)@MIL-101 for the CO2 capture and improving the catalytic CO2 conversion with epoxide, J. Colloid Interface Sci. 618 (2022) 22–33.
[26] W. Qian, J. Texter, F. Yan, Frontiers in poly(ionic liquid)s: syntheses and applications, Chem. Soc. Rev. 46 (4) (2017) 1124–1159.
[27] T.M. Ukarde, J.S. Mahale, P.H. Pandey, A. Vasishta, A.M.J.C. Harrish, H.S. Pawar, Facile Synthesis of Novel Polyethyleneimine Functionalized Polymeric Protic Ionic Liquids (PolyE-ILs) with Protagonist Properties for Acid Catalysis, ChemistrySelect 6 (36) (2021) 9616–9624.
[28] K. Manojkumar, K.T. Prabhu Charan, A. Sivaramakrishna, P.C. Jha, V.M. Khedkar, R. Siva, G. Jayaraman, K. Vijayakrishna, Biophysical Characterization and Molecular Docking Studies of Imidazolium Based Polyelectrolytes–DNA Complexes: Role of Hydrophobicity, Biomacromolecules 16 (3) (2015) 894–903.
[29] K. Manojkumar, D. Mecerreyes, D. Taton, Y. Gnanou, K. Vijayakrishna, Self-assembly of poly(ionic liquid) (PIL)-based amphiphilic homopolymers into vesicles and supramolecular structures with dyes and silver nanoparticles, Polym. Chem. 8 (22) (2017) 3497–3503.
[30] W. Zhang, Z. Kochovski, Y. Lu, B.V.K.J. Schmidt, M. Antonietti, J. Yuan, Internal Morphology-Controllable Self-Assembly in Poly(Ionic Liquid) Nanoparticles, ACS Nano 10 (8) (2016) 7731–7737.
[31] M. Koebe, M. Drechsler, J. Weber, J. Yuan, Crosslinked Poly(ionic liquid) Nanoparticles: Inner Structure, Size, and Morphology, Macromol. Rapid Commun. 33 (8) (2012) 646–651.
[32] E.J. Cornel, J. Jiang, S. Chen, J. Du, Principles and characteristics of polymerization-induced self-assembly with various polymerization techniques, CCS Chemistry 3 (4) (2021) 2104–2125.
[33] X. Zhou, J. Weber, J. Yuan, Poly(ionic liquid)s: Platform for CO2 capture and catalysis, Curr. Opin. Green Sust. 16 (2019) 39–46.
[34] Y. Xie, J. Liang, Y. Fu, M. Huang, X. Xu, H. Wang, S. Tu, J. Li, Hypercrosslinked mesoporous poly(ionic liquid)s with high ionic density for efficient CO2 capture and conversion into cyclic carbonates, J. Mater. Chem. A 6 (15) (2018) 6660–6666.
[35] E. Ewins, R.B. Lira, W. Zhang, J. Yuan, M. Antonietti, T. Robinson, R. Dimova, Poly(Ionic Liquid) Nanoparticles Selectively Disrupt Biomembranes, Adv. Sci. 6 (4) (2019) 1801602.
[36] I. Sullivan, A. Goryachev, I.A. Digdaya, X. Li, H.A. Atwater, D.A. Vermaas, C. Xiang, Coupling electrochemical CO2 conversion with CO2 capture, Nat. Catal. 4 (11) (2021) 952–958.
[37] M. Jouny, W. Luc, F. Jiao, General Techno-Economic Analysis of CO2 Electrolysis Systems, Ind. Eng. Chem. Res. 57 (6) (2018) 2165–2177.
[38] R. Sen, A. Goeppert, S. Kar, G.K.S. Prakash, Hydroxide Based Integrated CO2 Capture from Air and Conversion to Methanol, J. Am. Chem. Soc. 142 (10) (2020) 4544–4549.
[39] A.J. Garza, A.T. Bell, M. Head-Gordon, Mechanism of CO2 Reduction at Copper Surfaces: Pathways to C2 Products, ACS Catal. 8 (2) (2018) 1490–1499.
[40] Y.A. Alsunni, A.W. Alherz, C.B. Musgrave, Electrocatalytic Reduction of CO2 to CO over Ag(110) and Cu(211) Modeled by Grand-Canonical Density Functional Theory, J. Phys. Chem. C 125 (43) (2021) 23773–23783.
[41] D. Kim, C.S. Kley, Y. Li, P. Yang, Copper nanoparticle ensembles for selective electroreduction of CO2 to C2–C3 products, Proc. Nat. Acad. Sci. 114(40) (2017) 10560-10565.
[42] D. Raciti, C. Wang, Recent Advances in CO2 Reduction Electrocatalysis on Copper, ACS Energy Lett. 3 (7) (2018) 1545–1556.
[43] Z. Gu, H. Shen, L. Shang, X. Lv, L. Qian, G. Zheng, Nanostructured Copper-Based Electrocatalysts for CO2 Reduction, Small Methods 2 (11) (2018) 1800121.
[44] S. Nitopi, E. Bertheussen, S.B. Scott, X. Liu, A.K. Engstfeld, S. Horch, B. Seger, I.E. L. Stephens, K. Chan, C. Hahn, J.K. Nørskov, T.F. Jaramillo, I. Chorkendorff, Progress and Perspectives of Electrochemical CO2 Reduction on Copper in Aqueous Electrolyte, Chem. Rev. 119 (12) (2019) 7610–7672.
[45] Y. Ye, Y. Liu, Z. Li, X. Zou, H. Wu, S. Lin, Highly selective and active Cu-In2O3/C nanocomposite for electrocatalytic reduction of CO2 to CO, J. Colloid Interface Sci. 586 (2021) 528–537.
[46] W. Wang, S. Gong, J. Liu, Y. Ge, J. Wang, X. Lv, Ag-Cu aerogel for electrochemical CO2 conversion to CO, J. Colloid Interface Sci. 595 (2021) 159–167.
[47] X.-Q. Li, G.-Y. Duan, J.-W. Chen, L.-J. Han, S.-J. Zhang, B.-H. Xu, Regulating electrochemical CO2RR selectivity at industrial current densities by structuring copper@poly(ionic liquid) interface, Appl. Catal. B 297 (2021) 120471.
[48] K.T. Prabhu Charan, N. Pothanagandhi, K. Vijayakrishna, A. Sivaramakrishna, D. Mecerreyes, B. Sreedhar, Poly(ionic liquids) as "smart" stabilizers for metal nanoparticles, Eur. Polym. J. 60 (2014) 114–122.
[49] J.-K. Sun, Z. Kochovski, W.-Y. Zhang, H. Kirmse, Y. Lu, M. Antonietti, J. Yuan, General Synthetic Route toward Highly Dispersed Metal Clusters Enabled by Poly(ionic liquid)s, J. Am. Chem. Soc. 139 (26) (2017) 8971–8976.
[50] Y. Gong, H. Zhong, W. Liu, B. Zhang, S. Hu, R. Wang, General Synthetic Route toward Highly Dispersed Ultrafine Pd–Au Alloy Nanoparticles Enabled by Imidazolium-Based Organic Polymers, ACS App. Mater. Interfaces 10 (1) (2018) 776–786.
[51] D. Parida, C. Bakkali-Hassani, E. Lebraud, C. Schatz, S. Grelier, D. Taton, J. Vignolle, Tuning the activity and selectivity of polymerised ionic liquid-stabilised ruthenium nanoparticles through anion exchange reactions, Nanoscale 14 (12) (2022) 4635–4643.
[52] J. Yuan, M. Antonietti, Poly(ionic liquid) Latexes Prepared by Dispersion Polymerization of Ionic Liquid Monomers, Macromolecules 44 (4) (2011) 744–750.
[53] A. Khorsand Kheirabad, X. Pan, S. Long, Z. Kochovski, S. Zhou, Y. Lu, G. McInerney, J. Yuan, Colloidal dispersion of poly(ionic liquid)/Cu composite particles for protective surface coating against SAR-CoV-2, Nano Select 3 (1) (2022) 227–232.
[54] S. Stojkovikj, G.A. El-Nagar, F. Firschke, L.C. Pardo Pérez, L. Choubrac, M. Najdoski, M.T. Mayer, Electrocatalyst Derived from Waste Cu–Sn Bronze for CO2 Conversion into CO, ACS App. Mater. Interfaces 13 (32) (2021) 38161–38169.
[55] H. He, M. Zhong, B. Adzima, D. Luebke, H. Nulwala, K. Matyjaszewski, A Simple and Universal Gel Permeation Chromatography Technique for Precise Molecular Weight Characterization of Well-Defined Poly(ionic liquid)s, J. Am. Chem. Soc. 135 (11) (2013) 4227–4230.
[56] M. Krumrey, G. Ulm, High-accuracy detector calibration at the PTB four-crystal monochromator beamline, Nucl. Instruments Methods Phys. Res. Sect. A, Accelerators, Spectrometers, Detectors Associated Equipment (2001) 1175–1178. Medium: X; Size:.
[57] J. Wernecke, C. Gollwitzer, P. Muller, M. Krumrey, Characterization of an in-vacuum PILATUS 1M detector, J. Synchrotron Radiat. 21 (3) (2014) 529–536.
[58] A. Schavkan, C. Gollwitzer, R. Garcia-Diez, M. Krumrey, C. Minelli, D. Bartczak, S. Cuello-Nuñez, H. Goenaga-Infante, J. Rissler, E. Sjöström, G.B. Baur, K. Vasilatou, A.G. Shard, Number Concentration of Gold Nanoparticles in Suspension: SAXS and spICPMS as Traceable Methods Compared to Laboratory Methods, Nanomaterials 9 (4) (2019) 502.
[59] C. Gollwitzer, D. Bartczak, H. Goenaga-Infante, V. Kestens, M. Krumrey, C. Minelli, M. Pálmai, Y. Ramaye, G. Roebben, A. Sikora, Z. Varga, A comparison of techniques for size measurement of nanoparticles in cell culture medium, Anal. Methods 8 (26) (2016) 5272–5282.
[60] L.C. Pardo Pérez, A. Arndt, S. Stojkovikj, I.Y. Ahmet, J.T. Arens, F. Dattila, R. Wendt, A. Guilherme Buzanich, M. Radtke, V. Davies, K. Höflich, E. Köhnen, P. Tockhorn, R. Golnak, J. Xiao, G. Schuck, M. Wollgarten, N. López, M.T. Mayer,

Determining Structure-Activity Relationships in Oxide Derived Cu-Sn Catalysts During CO2 Electroreduction Using X-Ray Spectroscopy, Adv. Energy Mater. 12 (5) (2022) 2103328.
[61] Y.-L. Wang, B. Li, A. Laaksonen, Coarse-grained simulations of ionic liquid materials: from monomeric ionic liquids to ionic liquid crystals and polymeric ionic liquids, PCCP 23 (35) (2021) 19435–19456.
[62] Y.-L. Wang, Y.-L. Zhu, Z.-Y. Lu, A. Laaksonen, Electrostatic interactions in soft particle systems: mesoscale simulations of ionic liquids, Soft Matter 14 (21) (2018) 4252–4267.
[63] S.-C. Yang, B. Li, Y.-L. Zhu, A. Laaksonen, Y.-L. Wang, The ENUF method—Ewald summation based on nonuniform fast Fourier transform: Implementation, parallelization, and application, J. Comput. Chem. 41 (27) (2020) 2316–2335.
[64] Y.-L. Wang, A. Laaksonen, Z.-Y. Lu, Implementation of non-uniform FFT based Ewald summation in dissipative particle dynamics method, J. Comput. Phys. 235 (2013) 666.
[65] J. Yuan, S. Soll, M. Drechsler, A.H.E. Müller, M. Antonietti, Self-Assembly of Poly (ionic liquid)s: Polymerization, Mesostructure Formation, and Directional Alignment in One Step, J. Am. Chem. Soc. 133 (44) (2011) 17556–17559.
[66] Z. Kochovski, G. Chen, J. Yuan, Y. Lu, Cryo-Electron microscopy for the study of self-assembled poly(ionic liquid) nanoparticles and protein supramolecular structures, Colloid Polym. Sci. 298 (7) (2020) 707–717.
[67] I. Bressler, J. Kohlbrecher, A.F. Thunemann, SASfit: a tool for small-angle scattering data analysis using a library of analytical expressions, J. Appl. Cryst. 48 (5) (2015) 1587–1598.
[68] Z. Varga, Y. Yuana, A.E. Grootemaat, E. van der Pol, C. Gollwitzer, M. Krumrey, R. Nieuwland, Towards traceable size determination of extracellular vesicles, J. Extracell. Vesicles 3 (1) (2014) 23298.
[69] V. Delhorbe, D. Bresser, H. Mendil-Jakani, P. Rannou, L. Bernard, T. Gutel, S. Lyonnard, L. Picard, Unveiling the Ion Conduction Mechanism in Imidazolium-Based Poly(ionic liquids): A Comprehensive Investigation of the Structure-to-Transport Interplay, Macromolecules 50 (11) (2017) 4309–4321.
[70] R. Bleul, R. Thiermann, M. Maskos, Techniques To Control Polymersome Size, Macromolecules 48 (20) (2015) 7396–7409.
[71] T. Nishimura, Y. Sasaki, K. Akiyoshi, Biotransporting Self-Assembled Nanofactories Using Polymer Vesicles with Molecular Permeability for Enzyme Prodrug Cancer Therapy, Adv. Mater. 29 (36) (2017) 1702406.
[72] Z. Huang, M. Yi, Y. Liu, P. Qi, A. Song, J. Hao, Magnetic polymerizable surfactants: thermotropic liquid crystal behaviors and construction of nanostructured films, New J. Chem. 44 (38) (2020) 16537–16545.
[73] Y. Kimura, M. Takenaka, M. Ouchi, T. Terashima, Self-Sorting of Amphiphilic Block-Pendant Homopolymers into Sphere or Rod Micelles in Water, Macromolecules 53 (12) (2020) 4942–4951.
[74] Y. Kimura, T. Terashima, Morphology transition of amphiphilic homopolymer self-assemblies in water triggered by pendant design and chain length, Eur. Polym. J. 139 (2020) 110001.
[75] C. Barner-Kowollik, G.T. Russell, Chain-length-dependent termination in radical polymerization: Subtle revolution in tackling a long-standing challenge, Prog. Polym. Sci. 34 (11) (2009) 1211–1259.
[76] C. Gonzato, M. Semsarilar, E.R. Jones, F. Li, G.J.P. Krooshof, P. Wyman, O.O. Mykhaylyk, R. Tuinier, S.P. Armes, Rational Synthesis of Low-Polydispersity Block Copolymer Vesicles in Concentrated Solution via Polymerization-Induced Self-Assembly, J. Am. Chem. Soc. 136 (31) (2014) 11100–11106.
[77] M. Xiao, J. Liu, J. Yang, R. Wang, D. Xie, Biomimetic membrane control of block copolymer vesicles with tunable wall thickness, Soft Matter 9 (8) (2013) 2434–2442.
[78] Q. Ge, D. Lou, S. Lu, W. Zhang, L. Zhang, X. Wang, Aggregation behavior of N-alkyl imidazolium-based poly(ionic liquid)s in an organic solvent, RSC Adv. 6 (90) (2016) 87461–87468.
[79] A.V. Dobrynin, M. Rubinstein, Theory of polyelectrolytes in solutions and at surfaces, Prog. Polym. Sci. 30 (11) (2005) 1049–1118.
[80] A.V. Dobrynin, Effect of Counterion Condensation on Rigidity of Semiflexible Polyelectrolytes, Macromolecules 39 (26) (2006) 9519–9527.
[81] M. Satoh, J. Komiyama, T. Iijima, Counterion condensation in polyelectrolyte solution: a theoretical prediction of the dependences on the ionic strength and the degree of polymerization, Macromolecules 18 (6) (1985) 1195–1200.
[82] N.V. Brilliantov, D.V. Kuznetsov, R. Klein, Chain Collapse and Counterion Condensation in Dilute Polyelectrolyte Solutions, Phys. Rev. Lett. 81 (7) (1998) 1433–1436.
[83] G.-Y. Duan, X.-Q. Li, G.-R. Ding, L.-J. Han, B.-H. Xu, S.-J. Zhang, Highly Efficient Electrocatalytic CO2 Reduction to C2+ Products on a Poly(ionic liquid)-Based Cu0–CuI Tandem Catalyst, Angew. Chem. Int. Ed. 61 (9) (2022) e202110657.
[84] F. Hannig, G. Kehr, R. Fröhlich, G. Erker, Formation of chiral ionic liquids and imidazol-2-ylidene metal complexes from the proteinogenic aminoacid l-histidine, J. Organomet. Chem. 690 (24) (2005) 5959–5972.
[85] Z. Weng, Y. Wu, M. Wang, J. Jiang, K. Yang, S. Huo, X.-F. Wang, Q. Ma, G.W. Brudvig, V.S. Batista, Y. Liang, Z. Feng, H. Wang, Active sites of copper-complex catalytic materials for electrochemical carbon dioxide reduction, Nat. Commun. 9 (1) (2018) 415.
[86] Z. Weng, J. Jiang, Y. Wu, Z. Wu, X. Guo, K.L. Materna, W. Liu, V.S. Batista, G.W. Brudvig, H. Wang, Electrochemical CO2 Reduction to Hydrocarbons on a Heterogeneous Molecular Cu Catalyst in Aqueous Solution, J. Am. Chem. Soc. 138 (26) (2016) 8076–8079.